



NuSTAR and Keck Observations of Heavily Obscured Quasars Selected by *WISE*

Wei Yan¹, Ryan C. Hickox¹, Kevin N. Hainline², Daniel Stern³, George Lansbury⁴, David M. Alexander⁵,
Raphael E. Hviding², Roberto J. Assef⁶, David R. Ballantyne⁷, Michael A. Dipompeo¹, Lauranne Lanz¹,
Christopher M. Carroll¹, Michael Koss⁸, Isabella Lamperti⁹, Francesca Civano¹⁰, Agnese Del Moro¹¹,
Poshak Gandhi¹², and Adam D. Myers¹³

¹ Department of Physics and Astronomy, Dartmouth College, Hanover, NH 03755, USA; wei.yan.gr@dartmouth.edu

² Steward Observatory, University of Arizona, 933 North Cherry Avenue, Tucson, AZ 85721, USA

³ Jet Propulsion Laboratory, California Institute of Technology, 4800 Oak Grove Drive, Mail Stop 169-221, Pasadena, CA 91109, USA

⁴ Institute of Astronomy, University of Cambridge, Madingley Road, Cambridge CB3 0HA, UK

⁵ Department of Physics, University of Durham, South Road, Durham DH1 3LE, UK

⁶ Núcleo de Astronomía de la Facultad de Ingeniería, Universidad Diego Portales, Av. Ejército Libertador 441, Santiago, Chile

⁷ Center for Relativistic Astrophysics, School of Physics, Georgia Institute of Technology, Atlanta, GA 30332, USA

⁸ Eureka Scientific, Inc., 2452 Delmer Street Suite 100, Oakland, CA 946027 USA

⁹ Department of Physics and Astronomy, University College London, Gower Street, London WC1E 6BT, UK

¹⁰ Yale Center for Astronomy and Astrophysics, 260 Whitney Avenue, New Haven, CT 06520, USA

¹¹ Max Planck Institute for extraterrestrial Physics, Giessenbachstrasse 1, D-85748 Garching, Bayern, Deutschland, Germany

¹² Department of Physics and Astronomy, University of Southampton, Highfield, Southampton SO17 3RT, UK

¹³ Department of Physics and Astronomy, University of Wyoming, Laramie, WY 82071, USA

Received 2018 March 7; revised 2018 October 30; accepted 2018 November 2; published 2019 January 2

Abstract

A primary aim of the *Nuclear Spectroscopic Telescope Array* (*NuSTAR*) mission is to find and characterize heavily obscured Active Galactic Nuclei (AGNs). Based on mid-infrared photometry from the *Wide-Field Infrared Survey Explorer* (*WISE*) and optical photometry from the Sloan Digital Sky Surveys, we have selected a large population of luminous obscured AGNs (i.e., “obscured quasars”). Here we report *NuSTAR* observations of four *WISE*-selected heavily obscured quasars for which we have optical spectroscopy from the Southern African Large Telescope and W. M. Keck Observatory. Optical diagnostics confirm that all four targets are AGNs. With *NuSTAR* hard X-ray observations, three of the four objects are undetected, while the fourth has a marginal detection. We confirm that these objects have observed hard X-ray (10–40 keV) luminosities at or below $\sim 10^{43}$ erg s⁻¹. We compare X-ray and IR luminosities to obtain estimates of the hydrogen column densities (N_{H}) based on the suppression of the hard X-ray emission. We estimate N_{H} of these quasars to be at or larger than 10^{25} cm⁻², confirming that *WISE* and optical selection can identify very heavily obscured quasars that may be missed in X-ray surveys, and they do not contribute significantly to the cosmic X-ray background. From the optical Balmer decrements, we found that our three extreme obscured targets lie in highly reddened host environments. This galactic extinction cannot adequately explain the more obscured AGNs, but it may imply a different scale of obscuration in the galaxy.

Key words: galaxies: active – galaxies: nuclei – X-rays: galaxies

Supporting material: data behind figure

1. Introduction

Quasars are particularly luminous examples of Active Galactic Nuclei (AGNs). Unobscured (type 1) quasars have been well-studied ever since they were discovered over 50 years ago (Hazard et al. 1963; Schmidt 1963). Thanks to their high luminosities, unobscured quasars dominate over host galaxy light at most wavelengths, making them relatively easy to observe and study. However, it is now known that half or more of quasars are obscured by gas and dust (e.g., Hickox et al. 2007; Assef et al. 2013; Mateos et al. 2017). The existence of many obscured (type 2) quasars has direct implications for the growth history of supermassive black holes (SMBH) in galactic centers (e.g., Alexander & Hickox 2012; Hickox & Alexander 2018). Type 2 quasars also have implications for the origin of the cosmic X-ray background (CXB; Gilli et al. 2007a; Treister et al. 2009a; Ueda et al. 2014; Aird et al. 2015) and statistics of black hole growth across cosmic time. Some recent progress has suggested a large population of Compton-thick (CT) AGNs with intrinsic column densities of $N_{\text{H}} > 1.5 \times 10^{24}$ cm⁻² (e.g., Lansbury et al. 2015; Ricci et al. 2017a; Lanzuisi et al. 2018; Marchesi et al. 2018), as well as some contribution to the models of the CXB spectrum

(e.g., Comastri et al. 1995; Gilli et al. 2007b; Treister et al. 2009b; Draper & Ballantyne 2010; Ueda et al. 2014); however, this very obscuration makes the CT AGNs difficult to find and study. Therefore, identifying these heavily obscured quasars becomes important for a general understanding of black hole evolution (e.g., Gandhi et al. 2006).

Mid-infrared (IR) observations, in particular with the *Spitzer Space Telescope* and *Wide-Field Infrared Survey Explorer* (*WISE*), and X-ray surveys have now enabled us to detect significant samples of obscured quasars, as well as optical spectroscopy and photometry (e.g., Lacy et al. 2004; Stern et al. 2005; Hickox et al. 2007; Stern et al. 2012; Assef et al. 2013). However, many properties of obscured quasars still remain unknown. For example, CT sources comprise a large fraction of lower-luminosity AGNs (e.g., Goulding et al. 2012; Ricci et al. 2017b). While the CT fraction for more luminous quasars has important implications for their contribution to the CXB and galaxy evolution, few heavily obscured luminous quasars with intrinsic column densities over 10^{24} cm⁻² have been confirmed (e.g., Alexander et al. 2013; Gandhi et al. 2014).

X-ray observations of these heavily obscured quasars are challenging; for example, the photoelectric absorption cut-off (e.g., at around 10 keV for a $z = 0.2$ AGN absorbed by a column density of about 10^{24} cm^{-2}) dramatically reduces the flux of soft X-rays. This may bias the measured spectral parameters, such as the intrinsic power-law photon index Γ or N_{H} , if fitting spectra with low or a limited energy range. Also, CT levels of absorption deeply suppress the primary continuum, revealing strong Fe K α fluorescent line emission at 6.4 keV and a Compton reflection ‘‘hump’’ at $\sim 20\text{--}30$ keV (e.g., George & Fabian 1991).

Due to the limitations of observations, we have previously obtained only weak constraints on the distribution of the obscuring column density N_{H} of luminous quasars. For less powerful AGNs (i.e., Seyfert galaxies), the classic ‘‘unified model’’ is largely successful in explaining obscuration by varying viewing angles of the ‘‘torus’’ (Antonucci 1993; Urry & Padovani 1995; Netzer 2015). However, it remains unclear whether this picture also holds for powerful quasars. The observed dependence of AGN obscuration on observed luminosity suggests a departure from the simplest unified model (e.g., Ueda et al. 2003; Simpson 2005; Treister et al. 2010; Iwasawa et al. 2012; Assef et al. 2015; Buchner et al. 2015) and implicates and raises the possibility that a phase of heavy obscuration is important to process in galaxy evolution. The most powerful AGN may also be obscured by starbursts (e.g., Davies et al. 2007; Ballantyne 2008) or larger-scale gas clouds driven to the center of the galaxy by violent mergers or instabilities (e.g., Di Matteo et al. 2005; Hopkins et al. 2009; Brusa et al. 2015; Chen et al. 2015; DiPompeo et al. 2018). Different quasar fueling mechanisms can produce different distributions of N_{H} and CT fractions (e.g., Draper & Ballantyne 2012; Gohil & Ballantyne 2018a).

Due to recent deeper observations in the hard X-ray band (>10 keV) with the *Nuclear Spectroscopic Telescope Array* (*NuSTAR*; Harrison et al. 2013), we now can more accurately constrain the physical properties of obscured quasars (e.g., Lansbury et al. 2017). As the first orbiting observatory to focus high-energy X-rays, *NuSTAR* improves sensitivity by two orders of magnitude, as well as over an order of magnitude improvement in angular resolution relative to the previous generation of hard X-ray (>10 keV) observatories.

Based on mid-IR photometry from *WISE* and optical photometry from the Sloan Digital Sky Survey (SDSS), we have selected 40 obscured quasars (e.g., Hainline et al. 2014; DiPompeo et al. 2015a, 2016). Here, we use *NuSTAR* to probe the X-ray obscuration in a sample of these quasars at $z < 0.5$. We report Keck and *NuSTAR* observations of four *WISE*-selected heavily obscured quasars, for which Hainline et al. (2014) presented optical spectroscopy from the Southern African Large Telescope (SALT). The paper is organized as follows: Section 2 details the sample selection; Section 3 describes the Keck data analysis; Section 4 describes the *NuSTAR* data results. The results are discussed and summarized in Section 5. Throughout the paper, we assume a Λ CDM cosmology with $H_0 = 69.6 \text{ km s}^{-1} \text{ Mpc}^{-1}$, $\Omega_{\text{M}} = 0.286$, and $\Omega_{\Lambda} = 0.714$ (Wright 2006).

2. Obscured Quasar Sample

The parent population of 40 galaxies in total is drawn from Hainline et al. (2014), which were divided into two groups. Both groups are bright in the *WISE* 22 μm band ($W4 < 7$; Vega) and

optical ($20 < g < 22$) and use two slightly different *WISE* selection criteria for identifying obscured quasars. Using both *WISE* All-Sky and *AllWISE* photometry, these were selected to have mid-IR and optical colors characteristic of obscured quasars (Hickox et al. 2007; Stern et al. 2012). Objects of Group 1 are in the range $40^\circ < \text{R.A.} < 185^\circ$, $-2^\circ < \text{decl.} < 2^\circ$ with $W1 - W2 > 0.7$ and $7 \geq W4 \geq 6.5$, while those of Group 2 are $-2^\circ < \text{decl.} < 0^\circ$ with $W1 - W2 > 0.8$, $W4 \geq 7.0$, and $r_{\text{AB}} - W2_{\text{AB}} > 3.1$. In the parent population, the density on the sky is $\sim 0.07 \text{ deg}^{-2}$. The luminosities of these *WISE*-selected objects lie in a range of $\log(L_{8\mu\text{m}}/\text{erg s}^{-1}) = 44.0 - 45.0$, with an average (median) of $\langle \log(L_{8\mu\text{m}}/\text{erg s}^{-1}) \rangle = 44.9(44.8)$, while redshift has an average of $\langle z \rangle = 0.35$, with $z < 0.67$.

The photometric criteria used in the parent population (Hainline et al. 2014; DiPompeo et al. 2016) are relatively simple, and these sources are representative of large-scale, purely photometric statistical samples used, for example, for clustering studies to determine dark matter halo masses (Geach et al. 2013; DiPompeo et al. 2014, 2015b, 2017; Donoso et al. 2014). The SALT optical spectroscopy has confirmed the presence of 40 AGNs in the obscured quasar candidates observed in our program thus far (Hainline et al. 2014; Hviding et al. 2018), building on the success of an extensive spectroscopic survey of *Spitzer*-selected obscured quasar candidates (Lacy et al. 2013). Our SALT quasars are at relatively low redshift ($z < 0.5$) and their infrared spectral energy distributions (SEDs) indicate moderate quasar luminosities ($L_{\text{bol}} \sim 10^{45}\text{--}10^{46} \text{ erg s}^{-1}$). These targets are generally considered as typical obscured quasars; however, their gas-obscuring columns and contributions to the CXB remain unexplored due to a lack of sensitive high-energy X-ray observations.

In this study, we have targeted four objects from Group 1 for which fits to the latest SEDs done in this work indicate significant nuclear dust extinction, $A_V > 20$. These four targets J133331.15–012653.3, J130500.31+005422.1, J143459.27–014432.8, and J115158.63–004641.2 are broadly representative of the full Hainline et al. (2014) sample, but with an emphasis on the most heavily dust-reddened objects to maximize the likelihood of identifying Compton-thick sources. Examining SDSS images of these four selected targets, we found that J115158.63–004641.2 is a late-stage merger, while the remaining three are isolated galaxies. In our latest SED fitting, for simplicity we modeled the extinction as a screen along the line of sight. To check that this is at least a broadly realistic representation of the AGN emission, we compared it to other more sophisticated torus radiative transfer models (e.g., Silva et al. 2004; Siebenmorgen et al. 2015). We find that the broad shapes of our obscured AGN components are consistent with the output from these models for reasonable torus parameters and with a similar dependence on optical depth. The SALT spectra in Figure 1 have been calibrated on the basis of Keck spectra by the level of the continuum and some bright emission lines (e.g., [O II] and [Ne V]). The optical spectra indicate that all the targets are AGNs at $z < 0.5$, with moderate quasar-like luminosities ($L_{\text{bol}} \sim 10^{45}\text{--}10^{46} \text{ erg s}^{-1}$) according to the quasar luminosity function (e.g., Ueda et al. 2003), derived from their infrared SEDs (Hainline et al. 2014). Since the SALT spectra of these targets do not cover Hydrogen lines, Hainline et al. (2014) used the TBT (Trouille, Barger & Tremonti; Trouille et al. 2011) criterion (see Figure 7 in Hainline et al. 2014), which combines rest-frame $g\text{--}z$ color with the emission line ratio [Ne III]3869/[O III]3726,3729. TBT disentangles AGNs from star-forming (SF) galaxies and confirms that all our four targets are AGNs

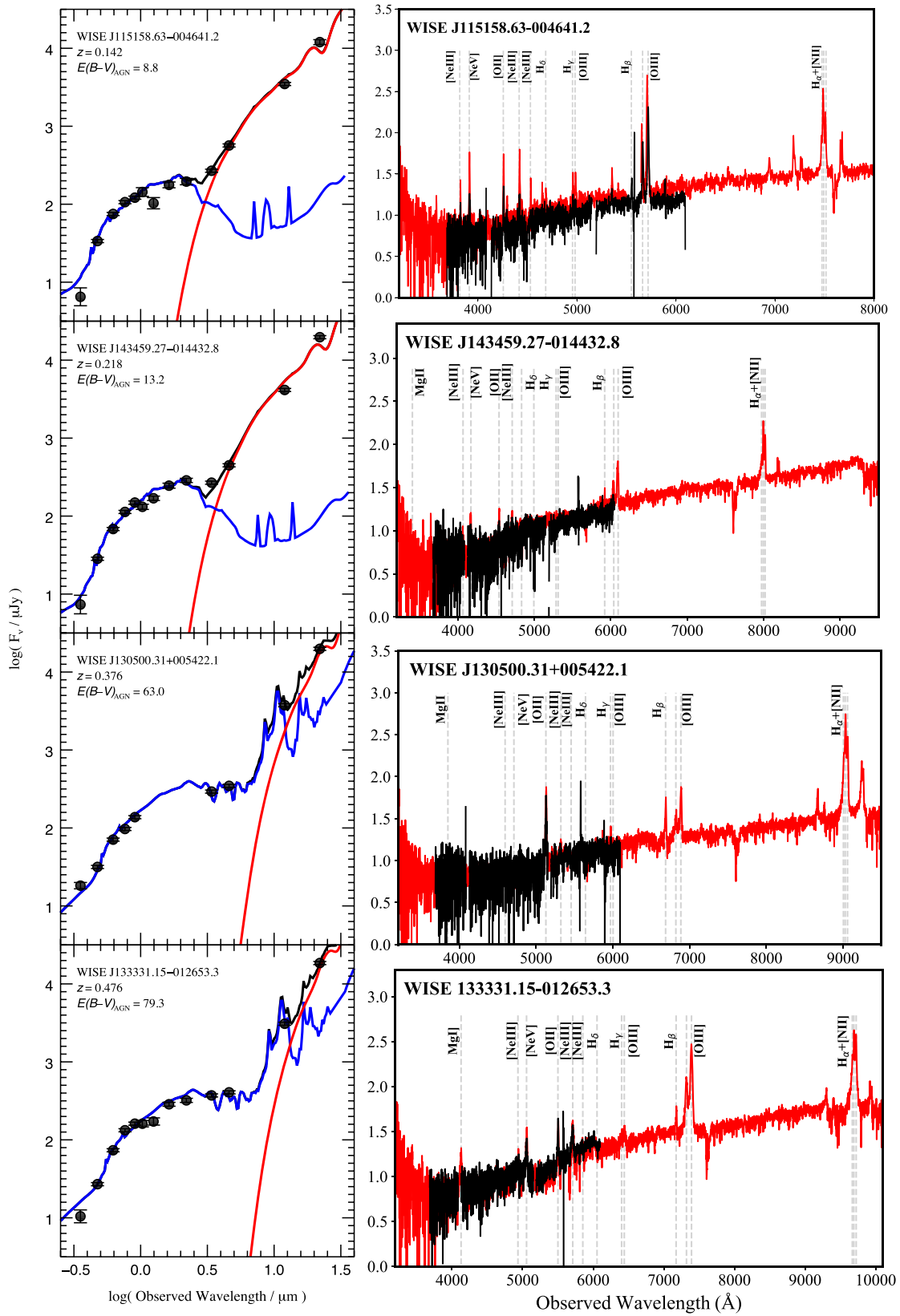


Figure 1. Spectral energy distributions (SEDs; left) and calibrated optical spectra from Keck (red lines) and SALT (black lines) in black solid lines respectively (right). The SALT spectra are calibrated on the basis of Keck spectra by the level of the continuum and some bright emission lines (e.g., [O II] and [Ne V]). The SEDs and spectra indicate that all of our targets are AGNs at moderate redshift, with moderate quasar-like luminosities ($L_{\text{bol}} \sim 10^{45} - 10^{46} \text{ erg s}^{-1}$) derived from their infrared spectra (Hainline et al. 2014). In their SEDs, the blue line is galaxy template fitted and the red line is AGN fitted. The SEDs indicates significant nuclear dust extinction of $A_V > 20$. Optical spectra from Keck show strong [O III] emission and large Balmer decrements, indicating relatively large obscuration on galactic scale. The data used to create this figure are available.

(Trouille et al. 2011). Most of our targets clearly lie in the upper right area, which is the high-excitation part of the diagram and well into the AGN regime.

Using the latest multi-component AGN and galaxy templates fit to the SEDs shown in Figure 1, we determined the intrinsic unobscured luminosity of the AGNs and the level of dust extinction. We have tried different template combinations and the systematic errors are small (~ 0.1 dex). These SED templates are the average results of the observations and are representative of the AGN population (Hickox et al. 2017). The AGN templates include Assef type 1 AGN template (Assef et al. 2008) and Richards et al. (2006) comparison template. Our selection of galaxy templates includes Assef elliptical template, Assef spiral template, Kirkpatrick et al. (2015) star-forming galaxy template, and Assef irregular template. Compared to the SED fittings to the same targets in Hainline et al. (2014), here we adopt more types of the latest AGNs and host galaxy templates and choose the best fits from these different combinations. This provides SED fitting that is less model-dependent and can be more easily compared to forthcoming work from our group (C. M. Carroll et al. 2018, in preparation). From the best SED fits shown in Figure 1, we obtained monochromatic intrinsic (unobscured and host corrected) infrared luminosities (νL_ν) at rest frame $6\ \mu\text{m}$ and $8\ \mu\text{m}$ for comparison to different results in the literature, assuming that the mid-IR provides a reliable tracer of the intrinsic AGN luminosity.

Here we follow the strategies of Stern et al. (2014) and Lansbury et al. (2014, 2015), applied to our new *WISE*-selected obscured quasars. *NuSTAR* has previously targeted specific samples of X-ray faint quasars selected through multiple techniques: luminous narrow-line “Type 2 quasars” at $z \sim 0.5$ selected with SDSS (Zakamska et al. 2003; Reyes et al. 2008; Lansbury et al. 2014, 2015); extremely luminous obscured objects at $z \sim 2$ identified with very red colors in *WISE* photometry (Eisenhardt et al. 2012; Stern et al. 2014; Ricci et al. 2017b); and broad absorption-line quasars identified through optical spectroscopy (Luo et al. 2013). The characteristics of these samples vary from one to another, and it is unclear how these targets fit into the full underlying obscured quasar population. Therefore it is important to select more “typical” quasars, like our four photometrically selected targets using infrared and optical data from *WISE* and SDSS (e.g., Hainline et al. 2014; DiPompeo et al. 2016).

We consider how our sample compares to the SDSS type 2 quasar sample, which is the basis for the previous estimate of the N_H distribution of obscured quasars (Lansbury et al. 2015). We use the SDSS sample (with W1, W2, W3, signal-to-noise ratio (S/N) > 3.0) presented in Reyes et al. (2008; see also Zakamska et al. 2003). The [O III] $\lambda 5007$ line is one of the indicators suitable for selecting a representative sample of obscured quasars to observe at X-ray energies. Since this emission line is one of the strongest visible in the optical at redshifts of about $z < 1$, it potentially ensures that the AGN selection has unbiased intrinsic luminosity. Reyes et al. (2008) includes 887 objects covering $10000\ \text{deg}^{-2}$. The density on the sky is about $0.08\ \text{deg}^{-2}$, similar to our parent *WISE*-selected sample. The sample has an average (median) of $\langle \log(L_{8\mu\text{m}}) \rangle = 44.7(44.3)$ while the upper limit of redshifts is set to be 0.84 ($\langle z \rangle = 0.324$, $z_{\text{median}} = 0.279$). Hence the sample in Reyes et al. (2008) and our parent group are comparable. Figure 2 shows that our parent group is generally

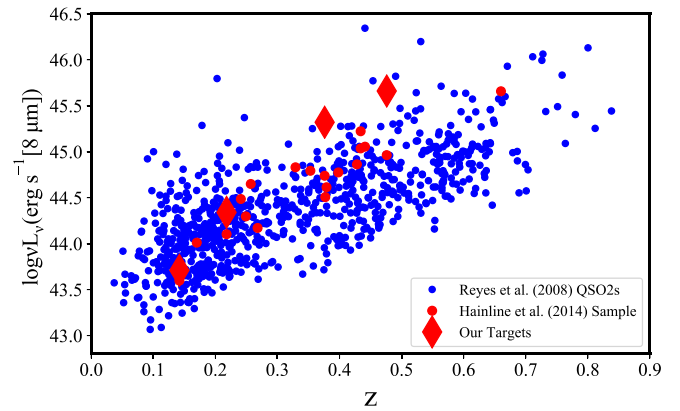


Figure 2. AGN luminosity at $8\ \mu\text{m}$ derived from SED fitting vs. spectroscopic redshift for selected samples. We show the SDSS Type 2 quasar sample from Reyes et al. (2008) in blue dots. The parent sample (Group 1 in Hainline et al. 2014) is shown as red dots and our four targets are shown as red diamonds. Two of our targets are AGNs with higher luminosities compared to those with similar redshifts.

comparable with the larger sample in Reyes et al. (2008) in redshift and luminosity.

3. Keck Observations and Results

Since our SALT observations cover a limited wavelength coverage ($\sim 3680\text{--}6100\ \text{\AA}$), we obtained follow-up optical spectra with broader wavelength and higher S/Ns. The spectra with limiting spectrograph resolution ($\approx \sigma = 100\ \text{km s}^{-1}$) were obtained during the night of 2017 April 28 (UT) at the W. M. Keck telescope with the Low Resolution Imaging Spectrograph (Oke et al. 1995). The exposure time varies from 300 to 450s.

We adopt the PYSPECKIT software to model the major emission lines at rest frame $3500\text{--}7000\ \text{\AA}$ (e.g., [Ne V], [O II], [Ne III], [He II] $4686\ \text{\AA}$, $H\beta$, [O III], [O I], $H\alpha$, [N II], [S II], see Table 1 for fluxes) following the general procedure in Koss et al. (2017). We first fit stellar emission using the penalized PiXel Fitting software (pPXF; Cappellari & Emsellem 2004) and the templates from the Miles Indo-U.S. Catalog (MIUSCAT) library of stellar spectra (Vazdekis et al. 2012). The MIUSCAT library of stellar spectra contains ≈ 1200 well-calibrated stars covering the spectral region of $3525\text{--}9469\ \text{\AA}$ at a spectral resolution of $2.51\ \text{\AA}$ (full width at half maximum, hereafter as FWHM). These spectra are used with an initial mass function to compute a slope of 1.3, considering a full range of metallicities ($M/H = -2.27$ to $+0.40$) and ages (0.03–14 Gyr). As these templates are observed at higher spectral resolution (FWHM = $2.51\ \text{\AA}$) than the AGN observations, they are convolved in pPXF to the spectral resolution of each observation before fitting. When fitting the stellar templates all of the prominent, emission lines are masked.

Based on the Keck spectra, we use the BPT (Baldwin et al. 1981; Kauffmann et al. 2003) diagram, to confirm that our targets are all AGNs. The position of the BPT diagram is defined on the basis of [O III] $\lambda 5007/H\beta$, [N II] $\lambda 6583/H\alpha$, and [S II] $\lambda\lambda 6716, 6731/H\alpha$ flux ratios (Baldwin et al. 1981), separating AGN from SF galaxies. In Figure 3, the solid blue curve is the theoretical boundary for the region occupied by starburst derived by the maximum starburst model from Kewley et al. (2001). The dashed line is the empirical SF line from Kauffmann et al. (2003), the dotted–dashed blue line is the empirical Seyfert–LINER (low ionization nuclear emission

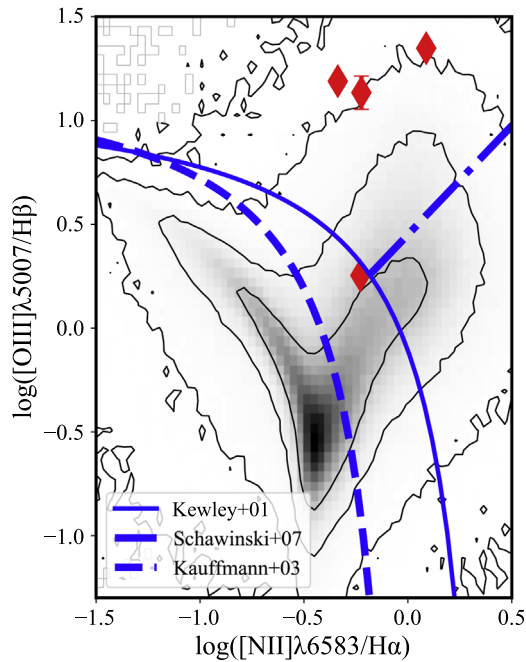


Figure 3. Optical excitation diagnostic (BPT) diagram to separate AGNs from star-forming galaxies using the fluxes from the Keck spectra. The solid blue curve is the theoretical boundary for the region occupied by starburst derived by the maximum starburst model from Kewley et al. (2001). The dashed line is the empirical SF line from Kauffmann et al. (2003). The dotted-dashed blue line is the empirical Seyfert-LINER separation from Schawinski et al. (2007). Red dots mark our targets. All of our targets lie in the AGN regime. For J1151-0046, $H\beta$ line was not measured in the Keck spectra because of falling in a gap between the blue and red CCD. Therefore, we use calibrated SALT flux for this line instead.

line regions) separation from Schawinski et al. (2007). Compared to the AGN sample in Reyes et al. (2008), we notice that our measured $[O III]$ luminosities are significantly lower (shown as gray in Figure 4). This indicates that there may be heavy absorption and the narrow-line emissions need further correction. For the Keck spectrum of WISE J115158.63-004641.2, the $H\beta$ line fell in the gap between the blue and red CCD, and so was not measured. However, there are clear $H\beta$ and $[O III]$ emission lines in the SALT spectrum (which we have otherwise not used for these line measurements because it covers a more limited wavelength range and does not have reliable absolute flux calibration). Therefore, we use the SALT spectrum to obtain the ratio of the fluxes of the $H\beta$ and $[O III]$ emission lines, by fitting Gaussian models to the two lines. We then multiply this ratio by the observed (and calibrated) $[O III]$ flux measured in Keck, to obtain an estimate of the flux in $H\beta$ for this target. The positions of all four targets on the BPT diagram are shown in Figure 3. WISE J130500.31+005422.1 is on the AGN/composite boundary in the BPT diagram, but its ratio of $[Ne III]/[O II]$ clearly identifies it as an AGN shown in Hainline et al. (2014). Therefore, we further confirm that our targets are all AGNs.

Since $[O III]$ can be used as the proxy of the intrinsic AGN power of obscured AGNs (e.g., Lamastra et al. 2009; Vignali et al. 2010), we obtained $[O III]$ luminosities of our targets, shown in Figure 4. We correct the narrow-line ratios ($H\alpha/H\beta$), assuming an intrinsic ratio of $R = 3.1$ and the Cardelli et al. (1989) reddening curve. We use the model presented in Charlot & Fall (2000) to correct the absorbed $[O III]$ luminosities by Balmer decrements and derive the host galactic extinction.

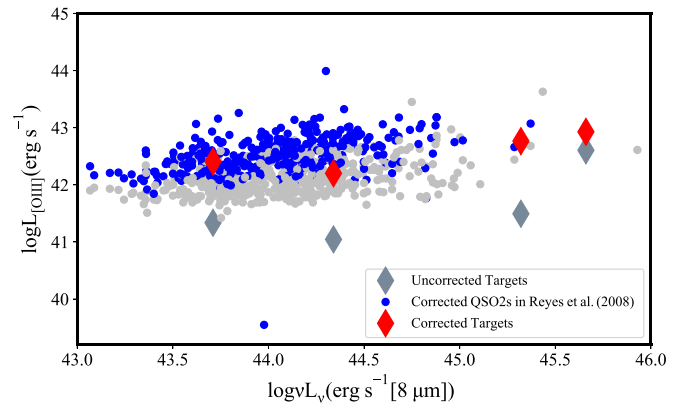


Figure 4. $[O III]$ luminosity plotted against infrared luminosity for the objects in selected samples. We show the reddening-corrected $[O III]$ and infrared luminosities for the SDSS Type 2 quasar sample from Reyes et al. (2008) in blue solid dots, excluding those without measured Balmer emissions. Red diamonds are our targets with corrected $[O III]$ luminosities. Gray dots and diamonds are those before correction. After correcting for reddening, our targets and the (Reyes et al. 2008) QSO2s lie in similar range of $L_{[O III]}$ and $L_{[8\mu m]}$.

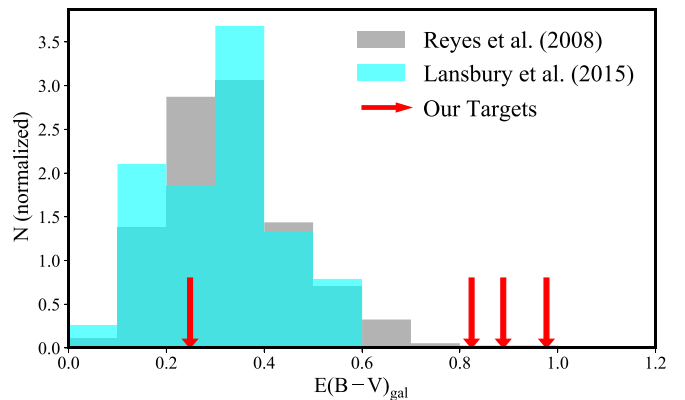


Figure 5. Distribution of reddening ($E(B - V)$) of QSO2s in the narrow-line region (NLR) at $z < 0.5$, obtained from the Balmer decrements. The histograms are normalized. Gray columns are host environments of SDSS sample presented in Reyes et al. (2008), while cyan ones are sources in Lansbury et al. (2014). Most of our targets lie around $0.8 < E(B - V) < 1.0$. In contrast, the extinction to the NLR of most QSO2s in previous samples is around 0.3, while our targets clearly show larger $E(B - V)$. This indicates that our targets are heavily obscured AGNs with dusty host galaxies.

Since the error from the fit of the emissions is generally less than 0.1%, the uncertainty of the corrected $[O III]$ flux mostly comes from the correction of the reddening curve, which is about 0.1 dex (Bosch et al. 2002). We then apply the same correction to our four targets and SDSS sample in Reyes et al. (2008). Since both $H\alpha$ and $H\beta$ emissions are required for this correction, we exclude those in Reyes et al. (2008) without measured Balmer emissions in Figure 4. After corrections, the $[O III]$ luminosities of our targets are comparable to those of the larger sample in Reyes et al. (2008), whose mid-IR luminosities are derived from SED fitting as well. However, the correlation in Figure 4 needs to be used with caution since the parameters space may not be valid for hyper-luminous QSOs (e.g., Hainline et al. 2016; Martocchia et al. 2017) or and the scattering is large at lower luminosities (e.g., Ueda et al. 2015).

Figure 5 compares the distribution of the host galactic extinction between our targets determined from the Balmer decrements, the Lansbury et al. (2015) sample and the Reyes

Table 1
Optical Emission Lines Observed with SALT and Keck

Object Name	H α (erg s $^{-1}$ cm $^{-2}$)	H β (erg s $^{-1}$ cm $^{-2}$)	[O III] (erg s $^{-1}$ cm $^{-2}$)	[N III] (erg s $^{-1}$ cm $^{-2}$)
J115158.63 – 004641.2	1.96	0.26 ^a	4.07	0.90
J143459.27 – 014432.8	0.46	0.06	0.78	0.27
J130500.31 + 005422.1	3.10	0.35	0.62	1.83
J133331.15 – 012653.3	0.79	0.21	4.61	0.97

Note.

^a This flux is calculated based on calibrated SALT data rather than Keck.

Table 2
WISE-Selected Obscured Quasar Targets

Object Name	z	$\log L_{6\mu\text{m}}$ (erg s $^{-1}$)	$\log L_{[\text{O III}]}$ (erg s $^{-1}$)	t_{exp} (ks)	$E(B - V)_{\text{AGN}}$
J115158.63 – 004641.2	0.142	43.9 \pm 0.1	41.3	40	8.8 \pm 1.5
J143459.27 – 014432.8	0.218	44.5 \pm 0.3	41.0	36	13.2 \pm 1.8
J130500.31 + 005422.1	0.376	45.4 \pm 0.1	41.5	26	63.0 \pm 9.7
J133331.15 – 012653.3	0.476	45.8 \pm 0.1	42.6	24	79.3 \pm 12.0

et al. (2008) sample. Most of our targets have $0.8 < E(B - V) < 1$, while most of those in other two samples have $0 < E(B - V) < 0.6$. This indicates that although we only selected our targets based on the extinctions in the nuclei, their host galaxies are heavily reddened. Therefore, our targets are more obscured on larger scales compared to other narrow-line quasar samples (e.g., Reyes et al. 2008; Lansbury et al. 2015), and these galaxies are among the dustiest galaxies found among typical X-ray selected AGNs, higher than almost all optically selected narrow-line AGNs (see Figure 12 in Koss et al. 2017 for distribution). We will discuss the extinctions of the nuclei in the following section.

We also attempted to obtain the velocity dispersion of our targets with Keck data. For the two most distant AGNs, WISE J130500.31+005422.1 and WISE J133331.15-012653.3, the low S/N and relatively weak features prevent a velocity dispersion measurement. In WISE J115158.63-004641.2 and WISE J143459.27-014432.8, both measurements are consistent with being at or below the limiting spectrograph resolution ($\approx \sigma = 100$ km s $^{-1}$). Further higher spectral resolution measurements are needed for firmer constraints.

4. *NuSTAR* Observations and Results

With *NuSTAR* observations, we are able to probe obscured quasars in the hard X-ray band to obtain constraints of the absorption by gas. We obtained *NuSTAR* images in each Focal Plane Module (FPMA and FPMB) of all four targets; the exposure times are listed in Table 2. To measure their brightness, we define regions of source and background as shown in Figure 6. We optimized the S/N ratio by using an aperture radius that encircles $\sim 50\%$ of the energy (29"; Harrison et al. 2013). We chose four to five background regions around each target that avoid the chip gaps. The radii of these regions are chosen to be larger than that of the target, and some of them lie on different chips in the *NuSTAR* FPMs from the target. We subtracted the backgrounds and calculate the net counts and errors of all 8 images in 3 bands (3–8 keV, 8–24 keV, 3–24 keV). The counting errors come from Poisson

statistics. Net counts and errors are in Table 3. We note that instrumental properties vary for different chips on the *NuSTAR* FPMs, so choosing background regions spanning different chips can, in principle, introduce some systematic uncertainty. However, we find that the surface brightnesses for the different background regions are consistent within Poisson errors, and choosing multiple large background regions allows us to minimize shot noise in estimating the background in the source region. We primarily focus on 3–24 keV because *NuSTAR* reaches maximum effective area within this energy range and collects photons most efficiently, which is very important for faint targets like ours when there are few photons at higher energies.

Following Lansbury et al. (2015), we calculated Poisson no-source probability (PB) at 3–24 keV for the four targets (Figure 7). We obtained a high PB for three of the four targets. Only the detected target J1434-0144 lies below 3σ PB after combining FPMA and FPMB. For those, we take 3σ as the upper limits determined using the prescription of Kraft et al. (2003) following Lansbury et al. (2015). We convert the *NuSTAR* count rate in the 3–24 keV band to luminosity in the rest frame 10–40 keV band, assuming a power-law spectrum with $\Gamma = 1.8$. By assuming different levels of N_{H} distribution (10^{22} – 10^{25} cm $^{-2}$) and Γ values (1.4–2.2), the conversion of the count rates into fluxes does not show significant differences once errors are taken into account. Therefore, we assume a non-absorption case for the X-ray calculations. These are presented in Table 3.

To study the level of X-ray obscuration in these objects, we first consider the intrinsic relationship between infrared and X-ray defined for unobscured (type 1) AGNs in Chen et al. (2017). We convert the 2–10 keV energy range used in Chen et al. (2017) into 10–40 keV luminosity again assuming a power-law spectrum with $\Gamma = 1.8$. Since we expect the targets to be heavily obscured, the level of obscuration may reach the limit of models like *MyTorus* (Murphy & Yaqoob 2009); therefore, we use the *BORUS02* model (Baloković et al. 2018), which is able to extend to $N_{\text{H}} \sim 10^{25.5}$ cm $^{-2}$ and determine the level of suppression of X-ray luminosities for column densities

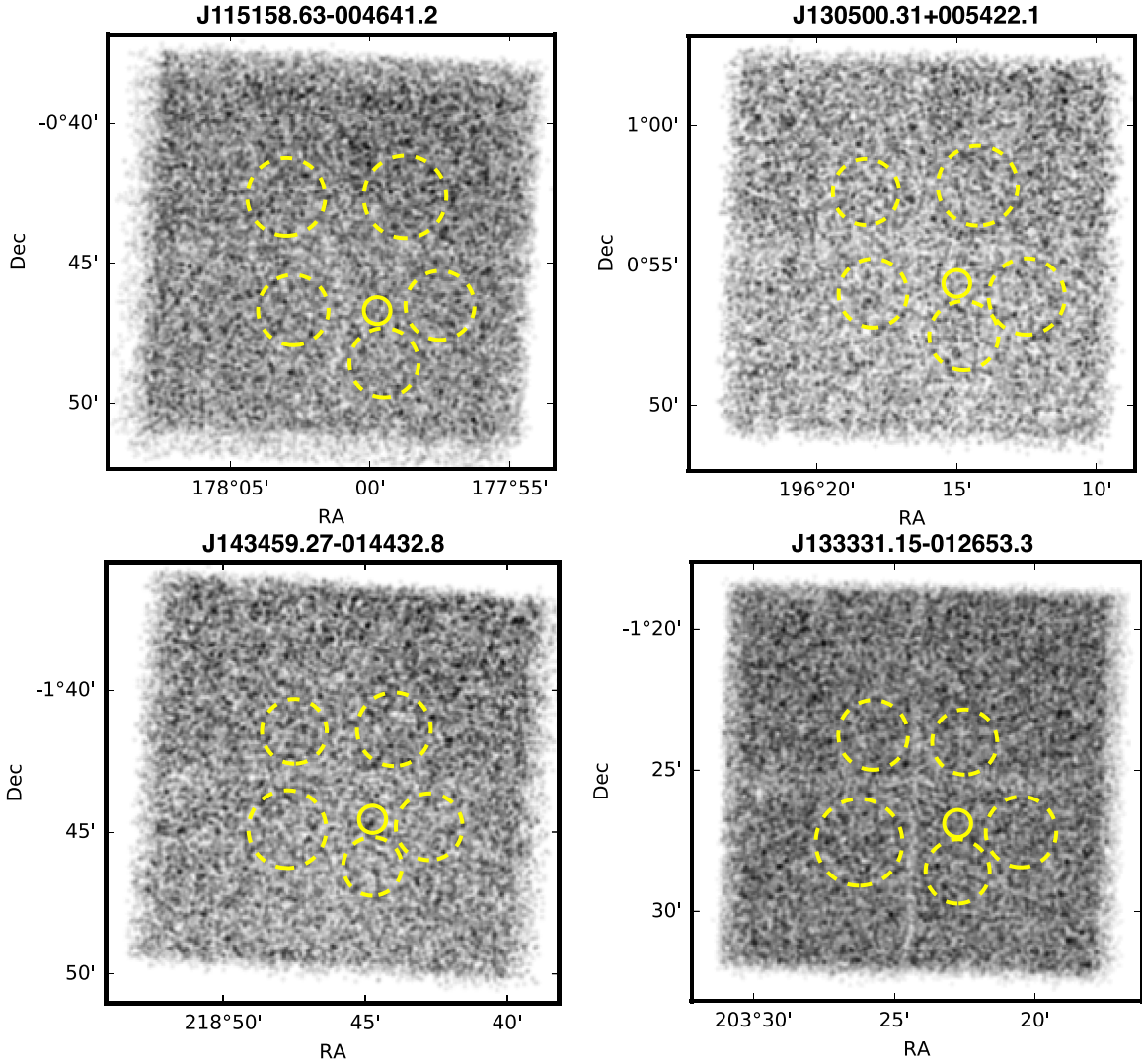


Figure 6. *NuSTAR* FPMA 3–24 keV X-ray images of our four obscured quasar targets with source (solid) and background (dashed) regions shown. Only one target J1434 – 0144 (lower left) is detected.

Table 3
Net Counts in 3–24 keV Band and Column Densities of Four Targets

Targets	Module A Net Counts	Module B Net Counts	Flux (10^{-15} erg s $^{-1}$ cm $^{-2}$)	$\log L_{10-40\text{keV}}$ (erg s $^{-1}$)	Column Density (10^{25} cm $^{-2}$)	$N_{\text{H}}/E(B-V)$ (10^{24} cm $^{-2}$)
J115158.63 – 004641.2	$-7.2 + 7.3^{\text{a}}$	$5.5 + 8.2^{\text{a}}$	$-1.1 + 7.8^{\text{a}}$	<42.1	>3.1	>3.5
J143459.27 – 014432.8	17.7 ± 7.9	29.6 ± 8.6	18.3 ± 9.2	42.4 ± 0.2	3.1	2.3 ± 0.4
J130500.31 + 005422.1	$-4.6 + 5.3^{\text{a}}$	$-0.7 + 5.7^{\text{a}}$	$-3.1 + 4.2^{\text{a}}$	<43.1	>3.1	>0.5
J133331.15 – 012653.3	$-14.2 + 8.6^{\text{a}}$	$5.9 + 9.4^{\text{a}}$	$-6.0 + 15.1^{\text{a}}$	<43.5	>1.0	>0.1

Note.

^a Positive uncertainties denote upper limits.

in the range between 1×10^{24} cm $^{-2}$ and 3.1×10^{25} cm $^{-2}$. In the overlapping column density range of validity (N_{H} up to $10^{25.5}$ cm $^{-2}$), we obtain similar results from *BORUS02* compared to *MYTORUS*.

The *BORUS02* model is a new Monte Carlo code simulating radiative transfer (details will be presented in M. Baloković et al. 2018, in preparation), which considers the interaction of the intrinsic X-ray continuum of AGNs with the surrounding medium. The model is applicable to a wide variety of AGNs (Baloković et al. 2018). Here we consistently take the photon

index as $\Gamma = 1.8$ to obtain the relation between X-ray and infrared luminosities with different column densities (Lansbury et al. 2015). Finally, we choose a redshift of $z = 0.3$ as the rough average redshift of our four targets. We set the inclination angle θ_{obs} between the line of sight and the symmetry axis of the torus as 60° as the average value of the area integral of the torus. After obtaining the ratio of X-ray to infrared luminosities of all the targets, based on the suppression, we estimate the range of column density where N_{H} of our targets fall. We then vary the column density along

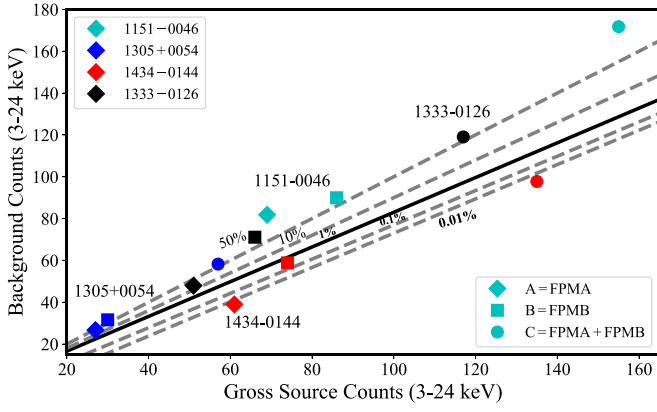


Figure 7. *NuSTAR* photometry (background counts vs. gross source counts) at 3–24 keV for our four targets. Background counts are determined based on the count density in background regions scaled to the source aperture. We adopted different constant Poisson no-source probability (Weisskopf et al. 2007) as the solid and dashed lines. Only the *NuSTAR*-detected target J1434-0144 has a significant detection.

the line of sight in the range between $1 \times 10^{24} \text{ cm}^{-2}$ and $3.1 \times 10^{25} \text{ cm}^{-2}$, which is the upper limit for the models, and derive the relationship between unabsorbed and absorbed luminosity for these column densities. Two representative relations with column densities of $3.1 \times 10^{24} \text{ cm}^{-2}$ and $3.1 \times 10^{25} \text{ cm}^{-2}$ are shown in Figure 8. Assuming a uniform density, to reach this level of obscuration, the mass would be unphysically high if distributed over too large a scale. Therefore, obscuration is typically found on small scales for extreme column densities. (Hickox & Alexander 2018).

From Figure 8, it is clear that our objects have absorbed hard (10–40 keV) X-ray luminosities at or below $\sim 10^{43} \text{ erg s}^{-1}$, with corresponding gas column densities N_{H} higher than 10^{25} cm^{-2} . We compute the ratios of X-ray to IR luminosities as a proxy for obscuration (e.g., Lansbury et al. 2015). The statistical error of the infrared luminosity is small enough to be neglected. Based on the observed spread of mid-IR SED shapes for a population of obscured quasars (e.g., Hickox et al. 2017), we estimate that the systematic error in our derived AGN luminosities due to the choice of SED template is about 0.1 dex. Since most of the X-ray luminosities are upper limits, it is possible that the actual column density value is higher than 10^{25} cm^{-2} . We repeat the same analysis above in different energy bands 3–8 keV and 8–24 keV and reach the same conclusions for the N_{H} estimate. By plotting the X-ray luminosities against the [O III] luminosities in Figure 9, we show that our targets also have X-ray luminosities well below the relation taken from LaMassa et al. (2010). This confirms that our targets are heavily obscured quasars with column densities above 10^{25} cm^{-2} . To be noticed, it is possible that at $z < 0.5$, about 17% to 40% optical-luminous quasars may have weak intrinsic X-ray luminosities (Luo et al. 2013) and do not follow the relations shown in Figure 9. However, since N_{H} values here agree with those derived from Figure 8, the low X-ray luminosities of our targets are more likely caused by heavy obscuration instead of weak intrinsic emission.

Since the sample of SDSS in Reyes et al. (2008) and our parent group are comparable as discussed in Section 2, we can make a direct comparison between their N_{H} distributions. To estimate N_{H} of all QSO2s in our parent sample, we only have one *NuSTAR*-detected target, so we adopt its ratio of N_{H} to $E(B - V)$ as fiducial for the sample. As its column density lies

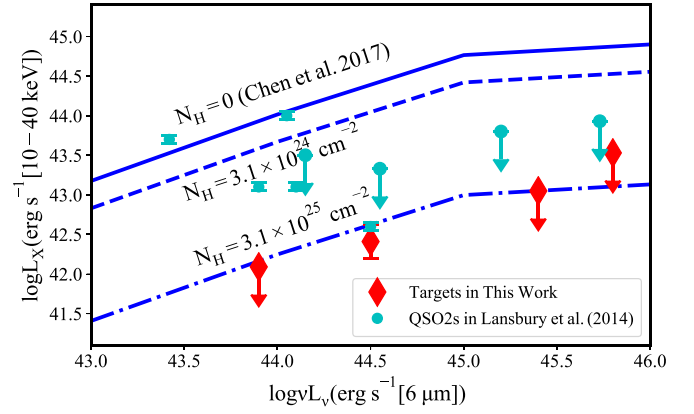


Figure 8. X-ray luminosity vs. infrared luminosity for obscured quasars. Red diamonds indicate our targets; Cyan dots indicate targets in Lansbury et al. (2015); the blue solid line is taken from a relationship of Chen et al. (2017) derived from unabsorption AGN. The blue dashed line is derived with *BORUS02* with a column density of $3.1 \times 10^{24} \text{ cm}^{-2}$, while the blue dotted-dashed line is of $3.1 \times 10^{25} \text{ cm}^{-2}$. The low observed hard X-ray luminosities imply very heavy obscuration in all four targets.

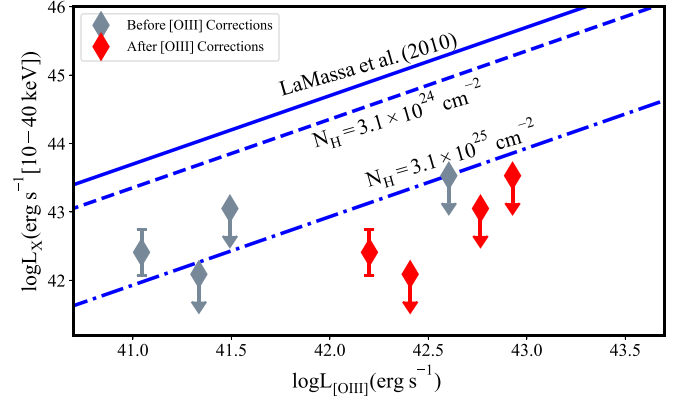


Figure 9. X-ray luminosity vs. [O III] luminosity for obscured quasars. Gray diamonds indicate our targets before [O III] luminosity corrections, while red diamonds indicate those with corrected [O III] luminosities; the blue solid line is taken from a relationship derived from unobscured AGNs in LaMassa et al. (2010).

close to $3.1 \times 10^{25} \text{ cm}^{-2}$, we take $3.1 \times 10^{25} \text{ cm}^{-2}$ for the estimation and $E(B - V) = 13.2$, which is derived from SED fitting. Therefore, we adopt 2.3×10^{24} as the value of “fiducial” gas-to-dust ratio. We then apply this value to 35 targets with known $E(B - V)$ values derived from our best SED fittings in this work and obtain an estimate of N_{H} of all these targets shown as red columns in Figure 10. Additionally, we compare our N_{H} distribution of QSO2s from X-ray spectral analysis to that of SDSS-selected QSO2s in Lansbury et al. (2015). From the comparison, our sample suggests a larger fraction of heavily obscured quasars at $N_{\text{H}} > 10^{25} \text{ cm}^{-2}$. As a result, the fraction of quasars that are Compton thick (f_{CT}) in our parent sample is $(45.5 \pm 12.1)\%$ with fiducial ratio, while f_{CT} in Lansbury et al. (2015) is $(32.5 \pm 11.5)\%$, which is $\sim 13\%$ (approximately 1σ) lower than ours. Considering the f_{CT} predicted by the nuclear starburst disks model (e.g., Gohil & Ballantyne 2018b), our distribution with fiducial ratio tends to be closer to the large fraction of the model prediction (f_{CT} around 60% for quasars).

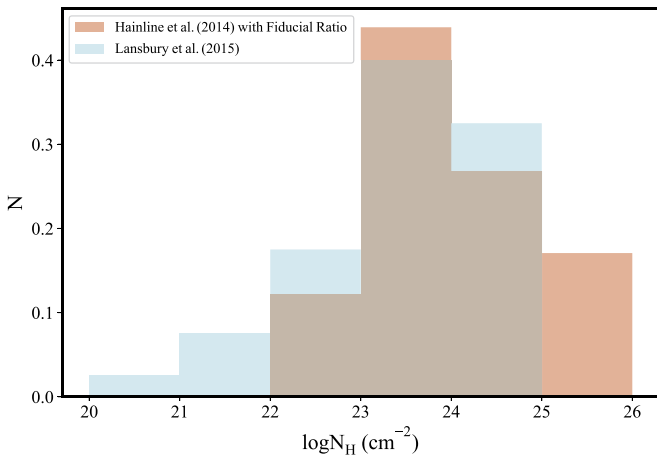


Figure 10. The *NuSTAR* N_H distribution of QSO2s at $z < 0.5$. The red histogram shows the distribution for *WISE*-selected QSO2s in Hainline et al. (2014), assuming for the gas-to-dust ratio the conservative value of $N_H/E(B - V)$ determined for our one *NuSTAR*-detected source. The cyan histogram shows the distribution for SDSS-selected QSO2s in Lansbury et al. (2015). Adopting the fiducial ratio, our *NuSTAR* targets all lie in the range between 25 and 26, and the distribution is skewed toward very high N_H . This indicates the potential existence of very heavily obscured quasars with column densities above 10^{25} cm^{-2} that may not have been identified in previous samples.

We also consider the gas-to-dust ratio of the Small Magellanic Cloud (SMC) as well, since AGNs with cold absorption in X-ray spectra as well as at least two broad lines in optical/IR spectra tend to have a gas-to-dust ratio similar to the SMC (Maiolino et al. 2001). In the SMC, the ratio of gas to dust, N_H/A_V , is about $2.2 \times 10^{22} \text{ atoms cm}^{-2} \text{ mag}^{-1}$ (Bohlin et al. 1978; Martínez-Sansigre et al. 2007; Burtscher et al. 2016). We parameterize the ratio of $N_H/E(B - V)$ based on typical reddening curves, i.e., SMC $R = A_V/E(B - V) = 2.7$, and adopt $N_H/E(B - V)$ of SMC as $6 \times 10^{22} \text{ cm}^{-2}$. We notice that the SMC gas-to-dust ratio is about one magnitude lower than our “fiducial” ratio. Therefore, if we adopt the SMC ratio instead of the “fiducial” ratio to estimate the N_H distribution of our parent sample, none of our selected sources have N_H above 10^{25} cm^{-2} . Since we have confirmed that at least four targets have a much higher obscuration level, we are underestimating the Compton-thick fraction with the SMC dust-to-gas ratio. This indicates that the SMC dust-to-gas ratio may not be applicable to quasars with the highest column density, i.e., one possibility is that dust sublimation on small scales in luminous AGNs causes relatively small dust columns compared to the column of gas (Elitzur & Netzer 2016).

Our analysis suggests that there may be a larger fraction of heavily-obscured quasars than is currently known. Although we use the single detected object to determine the column density in the ratio of $N_H/E(B - V)$, this detected X-ray source is the most conservative approach since other three targets might have a much larger column density. This points toward a possibility of an even larger fraction of heavily obscured quasars and may shed light on the composition of the obscuring material in heavily obscured quasars. Meanwhile, it is also possible that we are indeed underestimating the dust reddening due to the fact that the high column density cannot be simply explained by the screen obscuration. In this case, a lower $E(B - V)$ that is obtained by our SED fitting methods would lead to a higher observed ratio of gas to dust.

5. Discussion and Summary

We report *NuSTAR* hard X-ray observations of four targets belonging to a large population of 40 heavily obscured quasars selected by *WISE* based on mid-IR photometry. All the targets are quasars with L_{bol} around $10^{45} \text{ erg s}^{-1}$ at $z < 0.5$. The optical spectroscopy is from SALT and Keck, while the X-rays observations are from *NuSTAR*. Three out of four objects are too faint to be detected in the hard X-rays with *NuSTAR*, while the other one has only a marginal detection. From the upper limit and net counts of our X-ray observations in different bands, we confirm that our objects have observed X-ray luminosities at or below $\sim 10^{43} \text{ erg s}^{-1}$. This corresponds to gas column densities at or above 10^{25} cm^{-2} derived from L_X and $L_{6\mu\text{m}}$, confirming that *WISE* and optical selection can identify very heavily obscured quasars that may be missed in X-ray surveys. This also suggests the potential existence of many heavily obscured AGN with column densities over 10^{25} cm^{-2} . The repeated Compton scattering in X-ray band makes it difficult to detect heavily obscured AGNs (Wilman & Fabian 1999; Ikeda et al. 2009). Although small groups of CT sources have been found with X-ray surveys like the XMM-COSMOS survey, only a few CT AGN candidates have been found with a large sample of sources (e.g., 67 out of 1855 in Lansbury et al. 2018b). Compared to Optical/mid-IR selection, X-ray selection requires specially designed spectral modeling (Lansbury et al. 2018b) and is less efficient. Additionally, due to the limited photon statistics in deep fields, X-ray surveys are likely to miss AGNs with extreme N_H like our targets (e.g., Ueda et al. 2014; Burtscher et al. 2016).

Considering the torus model for AGN structure, the column densities imply more clumpiness of line-of-sight column densities (Dullemond & van Bemmelen 2005; Nenkova et al. 2008; Hönig & Kishimoto 2010). Due to the heavy obscuration, it is difficult to constrain the parameters in the torus model. For example, we are only able to obtain the lower limits of the line-of-sight column densities. This restraint may complicate the model compositions that are not yet fully understood, including the covering factor and anisotropy of the torus (e.g., Netzer 2015). Additionally, while a large population of obscured AGNs could increase the total radiation density produced by SMBHs in BH synthesis models, the heavily obscured AGNs contribute little emission due to the extremely high N_H (e.g., Martínez-Sansigre & Taylor 2009; Novak 2013). Given the large obscuration of our targets, the marginal detection and non-detections in the X-ray imply that these powerful AGNs do not contribute to the CXB for BH synthesis models. (Hickox & Alexander 2018).

Based on the narrow-line reddening of our targets, the extinctions of host galaxies are fairly high in three out of four. One of the targets, WISE J130500.31+005422.1, is a late-stage merger with consistent large galactic absorption. Their Balmer decrements indicate substantial reddening in their host galaxies, which suggests the existence of different scales of obscuration in the heavily buried luminous AGNs. The galactic column densities are around 10^{23} cm^{-2} , compared to the nuclear N_H over $3.1 \times 10^{25} \text{ cm}^{-2}$ of these CT quasars. Although the heavily reddened host environment is still not adequate enough to explain the obscuration of these AGNs, this reasonably high galactic obscuration may suggest a connection between obscuration on different scales and may be associated with black hole galaxy co-evolution (e.g., Hickox & Alexander 2018).

This research has made use of the NuSTAR Data Analysis Software (NuSTARDAS) jointly developed by the ASI Science Data Center (ASDC, Italy) and the California Institute of Technology (USA). The data presented herein were obtained at the W. M. Keck Observatory, which is operated as a scientific partnership among the California Institute of Technology, the University of California and the National Aeronautics and Space Administration. The Observatory was made possible by the generous financial support of the W. M. Keck Foundation. The authors wish to recognize and acknowledge the very significant cultural role and reverence that the summit of Maunakea has always had within the indigenous Hawaiian community. We are most fortunate to have the opportunity to conduct observations from this mountain. Some of the observations reported in this paper were obtained with the Southern African Large Telescope (SALT). R.C.H. acknowledges support from NASA grant NNX15AP24G and National Science Foundation CAREER Award number 1554584. R.J.A. was supported by FONDECYT grant number 1151408.

ORCID iDs

Wei Yan  <https://orcid.org/0000-0001-9519-1812>
 Ryan C. Hickox  <https://orcid.org/0000-0003-1468-9526>
 Kevin N. Hainline  <https://orcid.org/0000-0003-4565-8239>
 Daniel Stern  <https://orcid.org/0000-0003-2686-9241>
 George Lansbury  <https://orcid.org/0000-0002-5328-9827>
 David M. Alexander  <https://orcid.org/0000-0002-5896-6313>
 Raphael E. Hviding  <https://orcid.org/0000-0002-4684-9005>
 Roberto J. Assef  <https://orcid.org/0000-0002-9508-3667>
 David R. Ballantyne  <https://orcid.org/0000-0001-8128-6976>
 Michael A. Dipompeo  <https://orcid.org/0000-0001-6788-1701>
 Lauranne Lanz  <https://orcid.org/0000-0002-3249-8224>
 Christopher M. Carroll  <https://orcid.org/0000-0003-3574-2963>
 Michael Koss  <https://orcid.org/0000-0002-7998-9581>
 Isabella Lamperti  <https://orcid.org/0000-0003-3336-5498>
 Poshak Gandhi  <https://orcid.org/0000-0003-3105-2615>

References

- Aird, J., Alexander, D. M., Ballantyne, D. R., et al. 2015, *ApJ*, **815**, 66
 Alexander, D. M., & Hickox, R. C. 2012, *NewAR*, **56**, 93
 Alexander, D. M., Stern, D., Del Moro, A., et al. 2013, *ApJ*, **773**, 125
 Antonucci, R. 1993, *ARA&A*, **31**, 473
 Assef, R. J., Eisenhardt, P. R. M., Stern, D., et al. 2015, *ApJ*, **804**, 27
 Assef, R. J., Kochanek, C. S., Brodwin, M., et al. 2008, *ApJ*, **676**, 286
 Assef, R. J., Stern, D., Kochanek, C. S., et al. 2013, *ApJ*, **772**, 26
 Baldwin, J. A., Phillips, M. M., & Terlevich, R. 1981, *PASP*, **93**, 5
 Ballantyne, D. R. 2008, *ApJ*, **685**, 787
 Baloković, M., Brightman, M., Harrison, F. A., et al. 2018, *ApJ*, **854**, 42
 Bohlin, R. C., Savage, B. D., & Drake, J. F. 1978, *ApJ*, **224**, 132
 Bosch, G., Terlevich, E., & Terlevich, R. 2002, *MNRAS*, **329**, 481
 Brusa, M., Bongiorno, A., Cresci, G., et al. 2015, *MNRAS*, **446**, 2394
 Buchner, J., Georgakakis, A., Nandra, K., et al. 2015, *ApJ*, **802**, 89
 Burtscher, L., Davies, R. I., Graciá-Carpio, J., et al. 2016, *A&A*, **586**, A28
 Cappellari, M., & Emsellem, E. 2004, *PASP*, **116**, 138
 Cardelli, J. A., Clayton, G. C., & Mathis, J. S. 1989, *ApJ*, **345**, 245
 Charlot, S., & Fall, S. M. 2000, *ApJ*, **539**, 718
 Chen, C.-T. J., Hickox, R. C., Alberts, S., et al. 2015, *ApJ*, **802**, 50
 Chen, C.-T. J., Hickox, R. C., Goulding, A. D., et al. 2017, *ApJ*, **847**, 145
 Comastri, A., Setti, G., Zamorani, G., & Hasinger, G. 1995, *A&A*, **296**, 1
 Davies, R. I., Müller Sánchez, F., Genzel, R., et al. 2007, *ApJ*, **671**, 1388
 Di Matteo, T., Springel, V., & Hernquist, L. 2005, *Natur*, **433**, 604
 DiPompeo, M. A., Bovy, J., Myers, A. D., & Lang, D. 2015a, *MNRAS*, **452**, 3124
 DiPompeo, M. A., Hickox, R. C., Carroll, C. M., et al. 2018, *ApJ*, **856**, 76
 DiPompeo, M. A., Hickox, R. C., Eftekharzadeh, S., & Myers, A. D. 2017, *MNRAS*, **469**, 4630
 DiPompeo, M. A., Hickox, R. C., & Myers, A. D. 2016, *MNRAS*, **456**, 924
 DiPompeo, M. A., Myers, A. D., Hickox, R. C., et al. 2015b, *MNRAS*, **446**, 3492
 DiPompeo, M. A., Myers, A. D., Hickox, R. C., Geach, J. E., & Hainline, K. N. 2014, *MNRAS*, **442**, 3443
 Donoso, E., Yan, L., Stern, D., & Assef, R. J. 2014, *ApJ*, **789**, 44
 Draper, A. R., & Ballantyne, D. R. 2010, *ApJL*, **715**, L99
 Draper, A. R., & Ballantyne, D. R. 2012, *ApJL*, **753**, L37
 Dullemond, C. P., & van Bemmell, I. M. 2005, *A&A*, **436**, 47
 Eisenhardt, P. R. M., Wu, J., Tsai, C.-W., et al. 2012, *ApJ*, **755**, 173
 Elitzur, M., & Netzer, H. 2016, *MNRAS*, **459**, 585
 Gandhi, P., Garcet, O., Disseau, L., et al. 2006, *A&A*, **457**, 393
 Gandhi, P., Lansbury, G. B., Alexander, D. M., et al. 2014, *ApJ*, **792**, 117
 Geach, J. E., Hickox, R. C., Bleem, L. E., et al. 2013, *ApJL*, **776**, L41
 George, I. M., & Fabian, A. C. 1991, *MNRAS*, **249**, 352
 Gilli, R., Comastri, A., & Hasinger, G. 2007a, *A&A*, **463**, 79
 Gilli, R., Comastri, A., & Hasinger, G. 2007b, *A&A*, **463**, 79
 Gohil, R., & Ballantyne, D. R. 2018a, *MNRAS*, **475**, 3543
 Gohil, R., & Ballantyne, D. R. 2018b, *MNRAS*, **475**, 3543
 Goulding, A. D., Alexander, D. M., Bauer, F. E., et al. 2012, *ApJ*, **755**, 5
 Hainline, K. N., Hickox, R. C., Carroll, C. M., et al. 2014, *ApJ*, **795**, 124
 Hainline, K. N., Hickox, R. C., Chen, C.-T., et al. 2016, *ApJ*, **823**, 42
 Harrison, F. A., Craig, W. W., Christensen, F. E., et al. 2013, *ApJ*, **770**, 103
 Hazard, C., Mackey, M. B., & Shimmings, A. J. 1963, *Natur*, **197**, 1037
 Hickox, R. C., & Alexander, D. M. 2018, *ARA&A*, **56**, 625
 Hickox, R. C., Jones, C., Forman, W. R., et al. 2007, *ApJ*, **671**, 1365
 Hickox, R. C., Myers, A. D., Greene, J. E., et al. 2017, *ApJ*, **849**, 53
 Hönig, S. F., & Kishimoto, M. 2010, *A&A*, **523**, A27
 Hopkins, P. F., Cox, T. J., Younger, J. D., & Hernquist, L. 2009, *ApJ*, **691**, 1168
 Hviding, R. E., Hickox, R. C., Hainline, K. N., et al. 2018, *MNRAS*, **474**, 1955
 Ikeda, S., Awaki, H., & Terashima, Y. 2009, *ApJ*, **692**, 608
 Iwasawa, K., Gilli, R., Vignali, C., et al. 2012, *A&A*, **546**, A84
 Kauffmann, G., Heckman, T. M., Tremonti, C., et al. 2003, *MNRAS*, **346**, 1055
 Kewley, L. J., Dopita, M. A., Sutherland, R. S., Heisler, C. A., & Trevena, J. 2001, *ApJ*, **556**, 121
 Kirkpatrick, A., Pope, A., Sajina, A., et al. 2015, *ApJ*, **814**, 9
 Koss, M., Trakhtenbrot, B., Ricci, C., et al. 2017, *ApJ*, **850**, 74
 Kraft, R. P., Vázquez, S. E., Forman, W. R., et al. 2003, *ApJ*, **592**, 129
 Lacy, M., Ridgway, S. E., Gates, E. L., et al. 2013, *ApJS*, **208**, 24
 Lacy, M., Storrie-Lombardi, L. J., Sajina, A., et al. 2004, *ApJS*, **154**, 166
 LaMassa, S. M., Heckman, T. M., Ptak, A., et al. 2010, *ApJ*, **720**, 786
 Lamastra, A., Bianchi, S., Matt, G., et al. 2009, *A&A*, **504**, 73
 Lansbury, G. B., Alexander, D. M., Aird, J., et al. 2017, *ApJ*, **846**, 20
 Lansbury, G. B., Alexander, D. M., Aird, J., et al. 2018b, *MNRAS*, **480**, 2578
 Lansbury, G. B., Alexander, D. M., Del Moro, A., et al. 2014, *ApJ*, **785**, 17
 Lansbury, G. B., Gandhi, P., Alexander, D. M., et al. 2015, *ApJ*, **809**, 115
 Lanzuisi, G., Civano, F., Marchesi, S., et al. 2018, arXiv:1803.08547
 Luo, B., Brandt, W. N., Alexander, D. M., et al. 2013, *ApJ*, **772**, 153
 Maiolino, R., Marconi, A., Salvati, M., et al. 2001, *A&A*, **365**, 28
 Marchesi, S., Ajello, M., Marcotullii, L., et al. 2018, *ApJ*, **854**, 49
 Martínez-Sansigre, A., Rawlings, S., Bonfield, D. G., et al. 2007, *MNRAS*, **379**, L6
 Martínez-Sansigre, A., & Taylor, A. M. 2009, *ApJ*, **692**, 964
 Martocchia, S., Piconcelli, E., Zappacosta, L., et al. 2017, *A&A*, **608**, A51
 Mateos, S., Carrera, F. J., Barcons, X., et al. 2017, *ApJL*, **841**, L18
 Murphy, K. D., & Yaqoob, T. 2009, *MNRAS*, **397**, 1549
 Nenkova, M., Sirocky, M. M., Nikutta, R., Ivezić, Ž., & Elitzur, M. 2008, *ApJ*, **685**, 160
 Netzer, H. 2015, *ARA&A*, **53**, 365
 Novak, G. S. 2013, arXiv:1310.3833
 Oke, J. B., Cohen, J. G., Carr, M., et al. 1995, *PASP*, **107**, 375
 Reyes, R., Zakamska, N. L., Strauss, M. A., et al. 2008, *AJ*, **136**, 2373
 Ricci, C., Assef, R. J., Stern, D., et al. 2017b, *ApJ*, **835**, 105
 Ricci, C., Bauer, F. E., Treister, E., et al. 2017a, *MNRAS*, **468**, 1273
 Richards, G. T., Lacy, M., Storrie-Lombardi, L. J., et al. 2006, *ApJS*, **166**, 470
 Schawinski, K., Thomas, D., Sarzi, M., et al. 2007, *MNRAS*, **382**, 1415
 Schmidt, M. 1963, *Natur*, **197**, 1040
 Siebenmorgen, R., Heymann, F., & Efstathiou, A. 2015, *A&A*, **583**, A120
 Silva, L., Maiolino, R., & Granato, G. L. 2004, *MNRAS*, **355**, 973

- Simpson, C. 2005, *MNRAS*, 360, 565
- Stern, D., Assef, R. J., Benford, D. J., et al. 2012, *ApJ*, 753, 30
- Stern, D., Eisenhardt, P., Gorjian, V., et al. 2005, *ApJ*, 631, 163
- Stern, D., Lansbury, G. B., Assef, R. J., et al. 2014, *ApJ*, 794, 102
- Treister, E., Natarajan, P., Sanders, D. B., et al. 2010, *Sci*, 328, 600
- Treister, E., Urry, C. M., & Virani, S. 2009a, *ApJ*, 696, 110
- Treister, E., Urry, C. M., & Virani, S. 2009b, *ApJ*, 696, 110
- Trouille, L., Barger, A. J., & Tremonti, C. 2011, *ApJ*, 742, 46
- Ueda, Y., Akiyama, M., Hasinger, G., Miyaji, T., & Watson, M. G. 2014, *ApJ*, 786, 104
- Ueda, Y., Akiyama, M., Ohta, K., & Miyaji, T. 2003, *ApJ*, 598, 886
- Ueda, Y., Hashimoto, Y., Ichikawa, K., et al. 2015, *ApJ*, 815, 1
- Urry, C. M., & Padovani, P. 1995, *PASP*, 107, 803
- Vazdekis, A., Ricciardelli, E., Cenarro, A. J., et al. 2012, *MNRAS*, 424, 157
- Vignali, C., Alexander, D. M., Gilli, R., & Pozzi, F. 2010, *MNRAS*, 404, 48
- Weisskopf, M. C., Wu, K., Trimble, V., et al. 2007, *ApJ*, 657, 1026
- Wilman, R. J., & Fabian, A. C. 1999, *MNRAS*, 309, 862
- Wright, E. L. 2006, *PASP*, 118, 1711
- Zakamska, N. L., Strauss, M. A., Krolik, J. H., et al. 2003, *AJ*, 126, 2125